REGULAR PAPER

High-resolution 3D phased-array imaging of fatigue cracks using piezoelectric and laser ultrasonic system (PLUS)

To cite this article: Yoshikazu Ohara *et al* 2022 *Jpn. J. Appl. Phys.* **61** SG1044

Japanese Journal of Applied Physics **61**, SG1044 (2022)
https://doi.org/10.35848/1347-4065/ac48cd

REGULAR PAPER

High-resolution 3D phased-array imaging of fatigue cracks using piezoelectric and laser ultrasonic system (PLUS)

Yoshikazu Ohara[1*], Marcel C. Remillieux[2], T. J. Ulrich[2], Serina Ozawa[1], Kosuke Tsunoda[1], Toshihiro Tsuji[1], and Tsuyoshi Mihara[1]

[1]*Department of Materials Processing, Tohoku University, Sendai, Miyagi 980-8579, Japan*
[2]*Los Alamos National Laboratory, Los Alamos, NM 87545, United States of America*

*E-mail: ohara@material.tohoku.ac.jp

Received November 2, 2021; revised December 8, 2021; accepted January 6, 2022; published online May 19, 2022

This paper reports the effectiveness of a novel imaging system, piezoelectric and laser ultrasonic system (PLUS), for the three-dimensional (3D) imaging of fatigue cracks with a high-resolution. The PLUS combines a piezoelectric transmitter and the two-dimensional (2D) mechanical scanning of a laser Doppler vibrometer, enabling the 2D matrix array with an ultra-multiple number of receiving points for 3D phased array imaging. After describing the principle and 3D imaging algorithm of PLUS, we show the fundamental 3D imaging capability of the PLUS in a flat-bottom-hole specimen with varying the number of receiving points under a fixed large receiving aperture. We then demonstrate that the PLUS with 4275 receiving points (i.e. 75 $\times$ 57) achieves high-resolution 3D imaging of a fatigue crack with a high signal-to-noise ratio, providing the outline of the fatigue crack geometry. We also discuss the effectiveness of the ultra-multiple receiving points for suppressing grating lobes and random noise.

1. Introduction

Fatigue cracks are severe defects since the generation of fatigue cracks can significantly decrease the material strength of aging structures and mechanical components. The accurate nondestructive measurement of fatigue cracks is indispensable to ensure safety and reliability. Among various nondestructive testing (NDT) methods, ultrasonic testing (UT)[1,2] is one of the most powerful techniques for practical application since ultrasound is highly sensitive to cracks. Recently, ultrasonic phased array (PA) has been widely employed to image internal defects, such as cracks, in industrial fields.[3,4] As illustrated in Fig. 1(a), typical PAs employ a linear array transducer[5] composed of multiple rectangular piezoelectric elements, of which the number ranges from 32 to 128. Such PAs produce a two-dimensional (2D) image, which is referred to as a B-scan image. One of the benefits of PAs is that one can intuitively recognize defects from B-scan images. Since crack depth is a critical parameter for the maintenance management of aging infrastructures, the accurate measurement of crack depth has been intensively studied.[6–17] On the other hand, fracture mechanics[18] indicates that crack depth can change in the crack-length direction.[19,20] However, B-scan images obtained by a linear array transducer give a spatially-averaged crack geometry over the elevation aperture of the linear array transducer.[19,20] Hence, such devices cannot obtain the detailed 3D geometries of fatigue cracks. To overcome this difficulty and develop a more sophisticated maintenance management of infrastructures, the high-resolution three-dimensional (3D) imaging method has long been desired. Such 3D imaging would also play a vital role in elucidating the mechanisms of crack initiation and propagation[21,22] in infrastructures and achieving the concept of digital twins in NDE4.0.[23]

To achieve this, the 3D PA system using a 2D matrix array transducer[3] has been a promising technology. As illustrated in Fig. 1(b), a 2D matrix array transducer typically comprises small square piezoelectric elements. Given that linear array transducers have elements ranging from 32 to 128, a 2D matrix array transducer should have more than 32 $\times$ 32 (i.e. 1024) elements to obtain high image resolution. However, such a PA system encounters prohibitive costs and technical difficulties. Hence, a piezoelectric 2D array transducer typically has the elements of less than 256 for NDT application,[24–27] although state-of-the-art medical ultrasonic imaging has used the piezoelectric matrix array transducer with ultra-multiple elements, e.g. 1024 elements.[28,29]

To achieve high-resolution 3D imaging for NDT, we previously proposed a novel PA system, the piezoelectric and laser system (PLUS).[30] The PLUS combines a piezoelectric transmitter and the 2D scanning of an LDV to simulate a 2D matrix array with ultra-multiple elements. This enables 3D PA imaging without using a piezoelectric 2D matrix array transducer. We examined the importance of a large receiving aperture in the PLUS for high-resolution 3D imaging.[30,31] We also demonstrated the fundamental performance of the PLUS for stress corrosion cracking. However, the effect of the number of receiving points under a fixed large receiving aperture and the usefulness of the PLUS for fatigue cracks have yet to be clarified.

This study investigates the importance of ultra-multiple receiving points in the PLUS for high-resolution 3D imaging. After the fundamental experiment in a specimen having a flat bottom hole (FBH), we demonstrate the effectiveness of the PLUS for the high-resolution 3D imaging of a fatigue crack. We also discuss the effectiveness of ultra-multiple receiving points and the exciting future applications of the PLUS.

2. Principle of PLUS

Figure 2 shows the schematic of the PLUS. In the PLUS, a 2D matrix array receiver based on the 2D scanning of an LDV is combined with a monolithic piezoelectric transmitter. A monolithic piezoelectric transducer on a wedge emits an ultrasonic wave into a specimen. The incident angle of the ultrasonic wave can be selected using a suitable wedge. When a region irradiated by the ultrasonic wave contains defects, the ultrasonic scatterings at the defects occur. An LDV that can measure an out-of-plane vibration receives the scattered waves at a small laser irradiation spot on the top

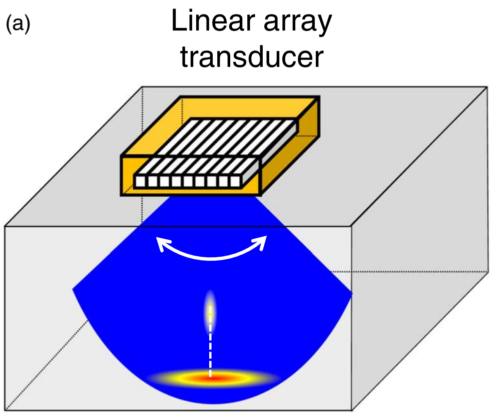

Fig. 1. (Color online) Schematics of phased array imaging. (a) 2D imaging with a linear array transducer. (b) 3D imaging with a 2D matrix array transducer.

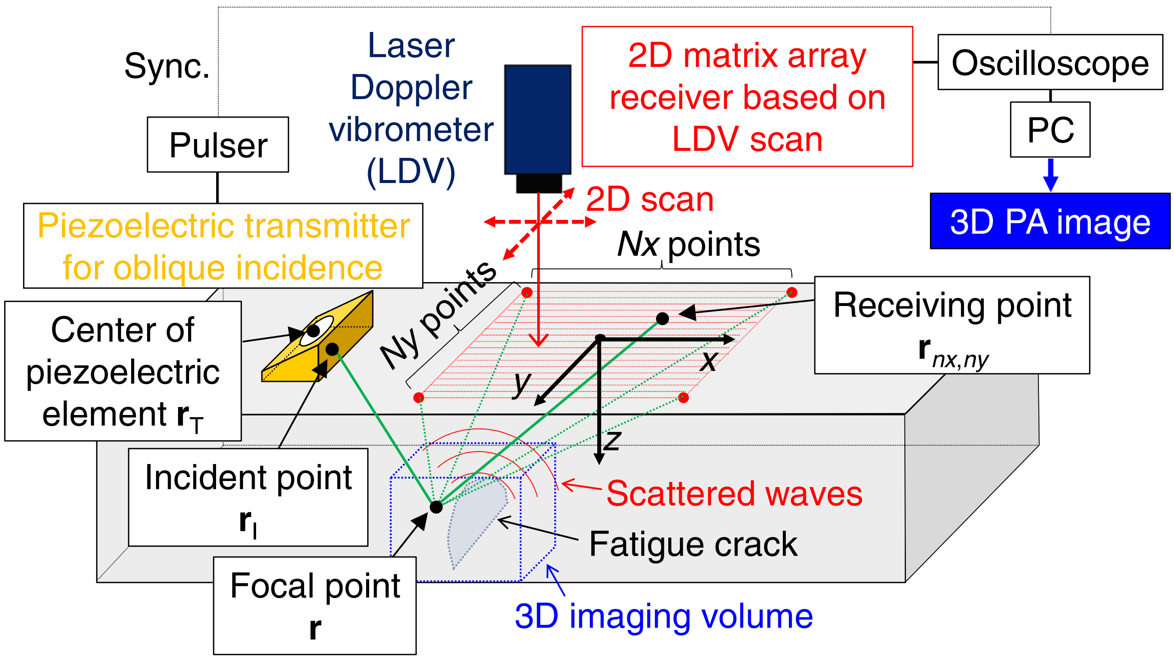

Fig. 2. (Color online) Schematic illustration of the PLUS.

surface. The received wave is transferred through an oscilloscope to a PC. By repeating this acquisition process at each receiving point over a scan area, a complete dataset of the received waves is stored on a PC. Subsequently, the dataset is post-processed to create the 3D image within a 3D imaging volume based on the imaging algorithm described later. Note that a 2D matrix array receiver based on the LDV scan can realize ultra-multiple receiving points (i.e. the order of thousands) with an arbitrary pitch, which is impossible for piezoelectric array transducers. Additionally, the PLUS using a monolithic piezoelectric transmitter can obtain a higher signal-to-noise ratio (SNR) than laser ultrasonics[32–34] because of the difference in the emission powers. Furthermore, the broad reception bandwidth of an LDV enables us to use an arbitrary frequency by selecting a suitable piezoelectric transmitter.

We describe the imaging algorithm for the PLUS. As shown in Fig. 2, we defined the origin in x–y–z Cartesian coordinates at the center of the LDV scan area. The propagation time from the transmitter through a point $\mathbf{r}$ to origin is given by

$$t_0(\mathbf{r}) = \frac{|\mathbf{r}_\mathrm{T} - \mathbf{r}_\mathrm{I}|}{V_\mathrm{W}} + \frac{|\mathbf{r}_\mathrm{I} - \mathbf{r}|}{V_i} + \frac{|\mathbf{r}|}{V_j}, \tag{1}$$

where $\mathbf{r}_\mathrm{T}$ is the center of the piezoelectric disk, $\mathbf{r}_\mathrm{I}$ is the incident point at the interface between the wedge and the specimen's top surface, V_W is the longitudinal wave speed in the wedge, and V_i and V_j are the speeds of the incident and scattered waves, respectively, in a specimen. Depending on an imaging condition, i and j are either L for a longitudinal wave or T for a transverse wave. Note that $t_0(\mathbf{r})$ is used as a reference. Likewise, the propagation time from the transmitter through $\mathbf{r}$ to the receiving point $\mathbf{r}_{nx,ny}$ is calculated as

$$t_{nx,ny}(\mathbf{r}) = \frac{|\mathbf{r}_\mathrm{T} - \mathbf{r}_\mathrm{I}|}{V_\mathrm{W}} + \frac{|\mathbf{r} - \mathbf{r}_\mathrm{I}|}{V_i} + \frac{|\mathbf{r}_{nx,ny} - \mathbf{r}|}{V_j}, \tag{2}$$

where nx and ny are the indices of the receiving point in the x- and y-directions, respectively. The delay law for each receiving point is obtained by subtracting $t_0(\mathbf{r})$ from $t_{nx,ny}(\mathbf{r})$;

$$\Delta t_{nx,ny}(\mathbf{r}) = t_{nx,ny}(\mathbf{r}) - t_0(\mathbf{r}) = \frac{|\mathbf{r}_{nx,ny} - \mathbf{r}| - |\mathbf{r}|}{V_j}. \quad (3)$$

As the imaging algorithm, delay-and-sum processing is used here. Assuming that the wave $u_{nx,ny}(t)$ is received at $\mathbf{r}_{nx,ny}$, the waveform after delay-and-sum processing for $\mathbf{r}$ is calculated as

$$U(\mathbf{r},\ t) = \frac{1}{N_x N_y} \sum_{nx=1}^{N_x} \sum_{ny=1}^{N_y} u_{nx,ny}(t - \Delta t_{nx,ny}(\mathbf{r})), \quad (4)$$

where N_x and N_y are the numbers of receiving points in the x- and y-directions, respectively. We then extract the scattering intensity for a voxel as the root mean square (RMS) of $U(\mathbf{r},\ t)$ using

$$I(\mathbf{r}) = \left(\frac{1}{\Delta\tau} \int_{t_0(\mathbf{r})}^{t_0(\mathbf{r})+\Delta\tau} U^2(\mathbf{r},\ t)\, dt \right)^{1/2}, \quad (5)$$

where $\Delta\tau$ is the temporal window for calculating the RMS value and is proportional to the length of the incident wave. By performing the above postprocessing for all $\mathbf{r}$ within a 3D imaging volume, we obtain a volumetric 3D image.

3. Experimental results

3.1. FBH specimen

For high-resolution 3D imaging, it is vital to select an appropriate imaging condition of the PLUS. We previously demonstrated that a large receiving aperture is indispensable to achieve high-resolution 3D imaging.[30,31] This is reasonable given the theoretical prediction of the lateral resolution of the images from Fourier optics;[35]

$$\Delta X \propto \lambda \frac{d}{a}, \quad (6)$$

where λ is the wavelength, d is the distance from the top surface, and a is the size of the receiving aperture. On the other hand, the importance of the number of receiving points on imaging results has yet to be clarified for a fixed receiving aperture in the PLUS. The small number of receiving points (i.e. a large scan pitch) can shorten the time required for the acquisition and postprocessing, whereas it causes the generation of grating lobes[5] and may deteriorate the quality of imaging results for other reasons.

To investigate the influence of the number of the receiving points on image quality in the PLUS, we made an FBH (ϕ3 mm, 10 mm height) in an aluminum-alloy (A5052) specimen. The thickness of the specimen was 39 mm. As shown in Fig. 3, we fixed a monolithic piezoelectric transmitter (5 MHz, ϕ12.7 mm) on an acrylic wedge to emit transverse waves at a refracted angle of 45°. Note that the use of a transverse wave can obtain a higher spatial resolution than that of a longitudinal wave since the wavelength of a transverse wave is shorter than that of a longitudinal wave.[35] The transmitter was set at the position 40 mm away from the center of an LDV scan area in the negative x-direction. The excitation voltage was a two-cycle square wave with a negative voltage of 200 V. We employed an LDV (OFV 505, Polytec) to receive the scattered waves at the top surface of the specimen. Note that the reception bandwidth of the LDV is flat between 0 and 20 MHz. The received signals digitized at a sampling rate of 250 MS s^{-1} were averaged five times with an oscilloscope and then transferred to the PC for the postprocessing. We carried out this acquisition process while scanning the LDV over a scan area of 31.5 mm × 31.5 mm, which corresponds to a large receiving aperture. We covered the scan area with a thin retroreflective tape to obtain sufficient laser reflectivity. In this study, we varied the scan pitch from 2 to 0.5 mm while the large receiving aperture of 31.5 mm × 31.5 mm was fixed. The number of receiving points were 256 (i.e. $N_x = N_y = 16$) [Fig. 3(b)], 462 (i.e. $N_x = N_y = 22$) [Fig. 3(c)], 1024 (i.e. $N_x = N_y = 32$) [Fig. 3(d)], and 4096 (i.e. $N_x = N_y = 64$) [Fig. 3(e)] for the scan pitch of 2.0, 1.5, 1.0, and 0.5 mm, respectively. Note that the 4096 receiving points are much more than the maximum number of elements for piezoelectric 2D matrix array transducers. After the data acquisition, we applied the postprocessing to the received waveforms to obtain 3D imaging results. The transverse wave speed V_T in the specimen was measured to be 3165 m s^{-1}, which was used as V_i and V_j in Eqs. (1)–(3). A 3D imaging volume was set to 26 mm × 26 mm × 26 mm with 0.5 mm steps in the x-, y-, and z-directions.

Figures 4(a), 4(c), 4(e), and 4(g) show 3D views of the imaging results obtained by the PLUS with 256, 462, 1024, and 4096 receiving points, respectively. Here, the responses of scattering intensity above a threshold were displayed. Note that we selected a threshold of 2.5×10^{-5} [i.e. a half of the maxmium value of the color scale for Figs. 4(b), 4(d), 4(f), and 4(h)] given the visibility of the 3D images. We also superimposed the semitransparent B-scan (yz-plane at $x = -21$ mm) images, which were extracted from the 3D imaging results and correspond to the plane in which the FBH existed. The B-scan images are also shown as opaque images in Figs. 4(b), 4(d), 4(f), and 4(h).

Regardless of the receiving points, the top of the FBH was visualized at the correct position. The spatial resolutions were comparable in all the imaging results. This is reasonable since the spatial resolution is determined by the receiving aperture and wavelength, as shown in Eq. (6). Also, a grating lobe was not prominent in the 3D imaging volume, even for the large scan pitch of 2 mm. This is because the position of the FBH was at the center of the 2D matrix array receiver in the y-direction, which is a position less sensitive to the generation of grating lobes,[5] and the 3D imaging volume was limited to 26 mm × 26 mm × 26 mm. On the other hand, the SNR markedly changed depending on the number of receiving points. Specifically, the noise level increased with decreasing the number of receiving points, although the response of the FBH was almost constant. In the FBH specimen, we could identify the response of the FBH from the imaging results. However, the decrease in SNR due to the small number of the receiving points would be a problem for visualization of cracks since the scatterings at cracks are much weaker than those at the FBH.

3.2. Fatigue-crack specimen

To demonstrate the usefulness of PLUS for the high-resolution 3D imaging of fatigue cracks, we performed a three-point bending test in an aluminum alloy (A7075) specimen to prepare a fatigue crack. The fatigue condition selected in this study was a maximum stress intensity factor of 5.3 MPa·$m^{1/2}$ and a minimum stress intensity factor of

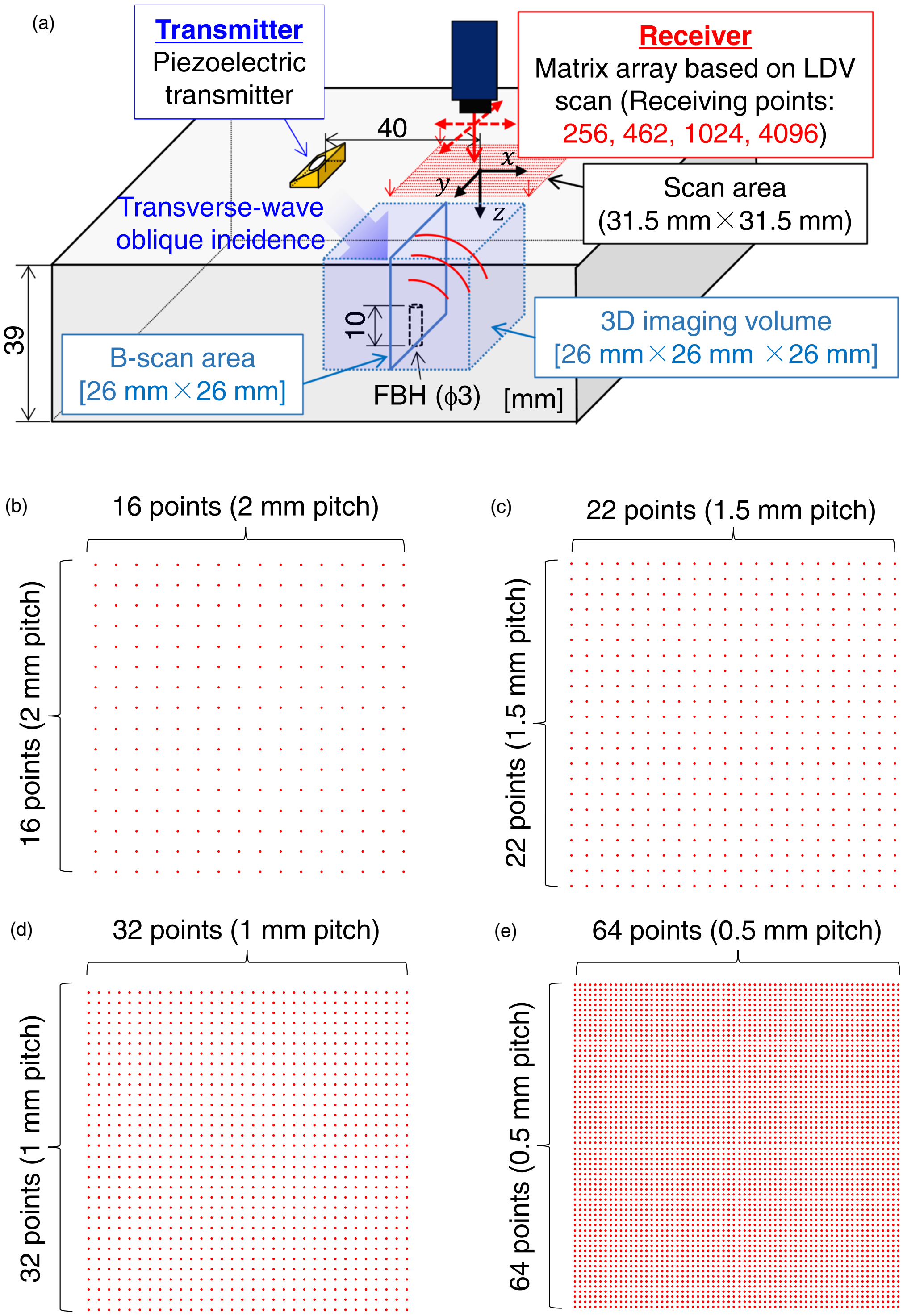

Fig. 3. (Color online) Experimental conditions for imaging the FBH by the PLUS. (a) Experimental configuration. Receiving points within the scan area of 31.5 mm × 31.5 mm: (b) 256, (c) 462, (d) 1024, and (3) 4096.

0.6 MPa·m$^{1/2}$.[6] Under this fatigue condition, we extended the fatigue crack from a starting notch to a depth of approximately 20 mm [Fig. 5(a)]. According to fracture mechanics,[18] the crack depth is not constant in the crack length direction (i.e. the y-direction). This is because of the change in the stress–strain fields around a crack tip in the crack length direction. The stress–strain fields can be approximated as plane-strain and plane-stress states in the center of the crack length direction and in the vicinity of the side surfaces, respectively. As a result, the tensile stress is larger in the center than in the vicinity of the side surfaces. Hence, the crack is deeper in the center than around the side surfaces, as schematically illustrated in Fig. 5(b).

Figure 5 shows the experimental conditions for imaging the fatigue crack. As shown in Fig. 5(a), we used the same transmitter employed in the experiment for imaging the FBH [Fig. 3(a)]. The transmitter was set at the position 38 mm away from the center of the LDV scan area in the negative x-direction. By exciting it by a square wave at a negative voltage of 150 V, an obliquely incident transverse wave was irradiated onto the fatigue crack. The scattered waves were received at the top surface of the specimen by the LDV. The

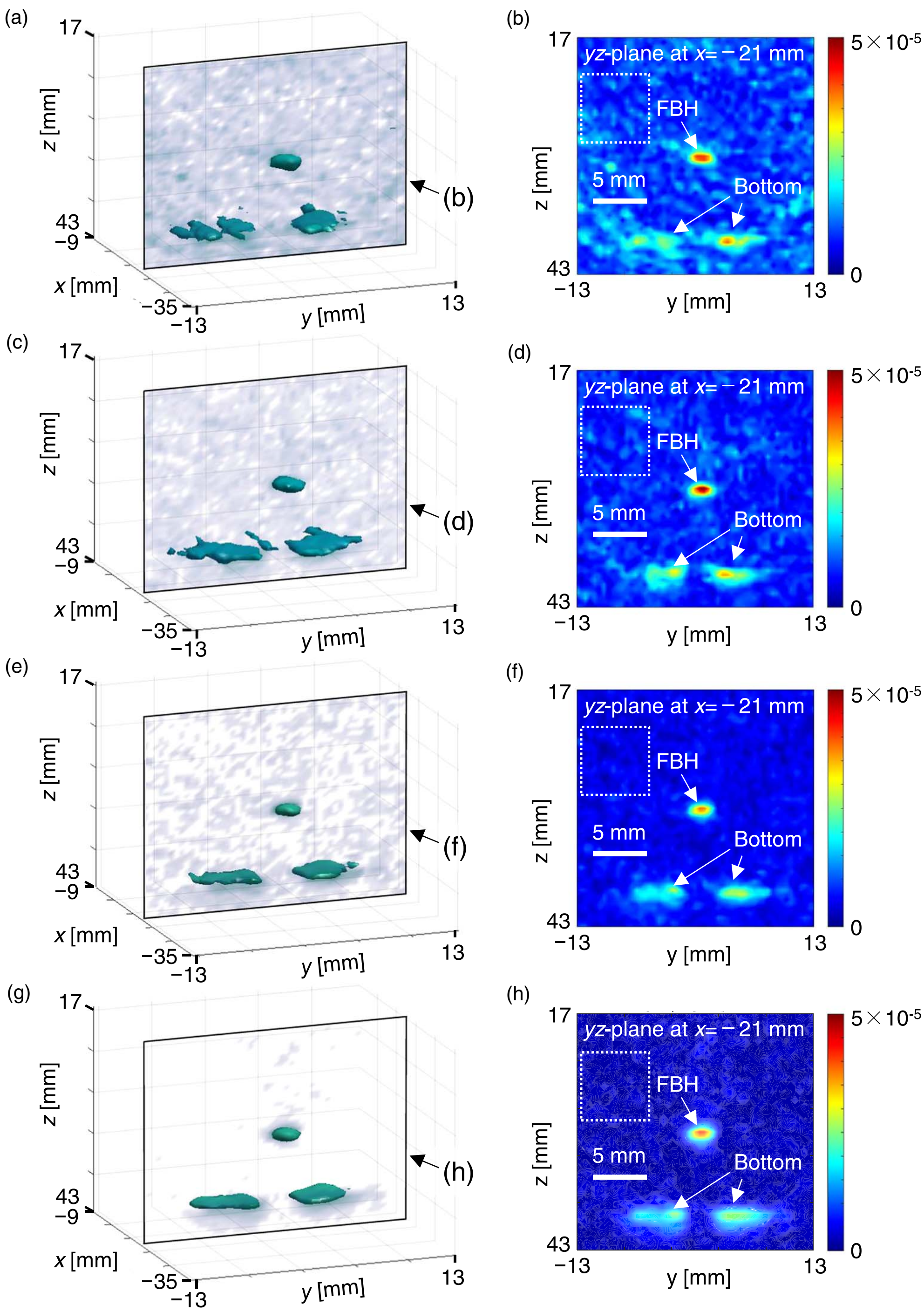

Fig. 4. (Color online) 3D imaging results of the FBH specimen obtained by the PLUS. (a) 3D view for 16 × 16 (i.e. 256 receiving points). (b) B-scan (yz-plane at $x = -21$ mm) image extracted from (a). (c) 3D view for 22 × 22 (i.e. 462 receiving points). (d) B-scan (yz-plane at $x = -21$ mm) image extracted from (c). (e) 3D view for 32 × 32 (i.e. 1024 receiving points). (f) B-scan (yz-plane at $x = -21$ mm) image extracted from (e). (g) 3D view for 64 × 64 (i.e. 4096 receiving points). (h) B-scan (yz-plane at $x = -21$ mm) image extracted from (g). The white dotted squares are the areas selected for obtaining the intensities of random noise.

received signals digitized at a sampling rate of 250 MS s^{-1} were averaged 64 times with an oscilloscope and then transferred to a PC for the postprocessing. We repeated this acquisition process while scanning the LDV over a scan area of 37 mm × 28 mm, which corresponds to a large receiving aperture. The scan area was covered with the retroreflective tape. Here, we varied the scan pitch from 2 to 0.5 mm while the large receiving aperture was fixed. The number of receiving points were 270 (i.e. N_x = 18, N_y = 15) [Fig. 5(c)], 475 (i.e. N_y = 19) [Fig. 5(d)], 1102 (i.e. N_x = 38, N_y = 29) [Fig. 5(e)], and 4275 (i.e. N_x = 75, N_y = 57) [Fig. 5(f)] for the scan pitch of 2.0, 1.5, 1.0, and 0.5 mm, respectively. We applied the postprocessing to the received waveforms to obtain 3D imaging results. The transverse wave speed V_T in the specimen was measured to be 3080 m s^{-1}, which was used as V_i and V_j in Eqs. (1)–(3). A 3D imaging volume was set to 26 mm × 26 mm × 26 mm with 0.5 mm steps in the x-, y-, and z-directions.

Figures 6(a), 6(c), 6(e), and 6(g) show 3D views of the imaging results obtained by PLUS with 270, 475, 1102, and 4275 receiving points, respectively. In the same manner as Fig. 4, we displayed the responses of scattering intensity

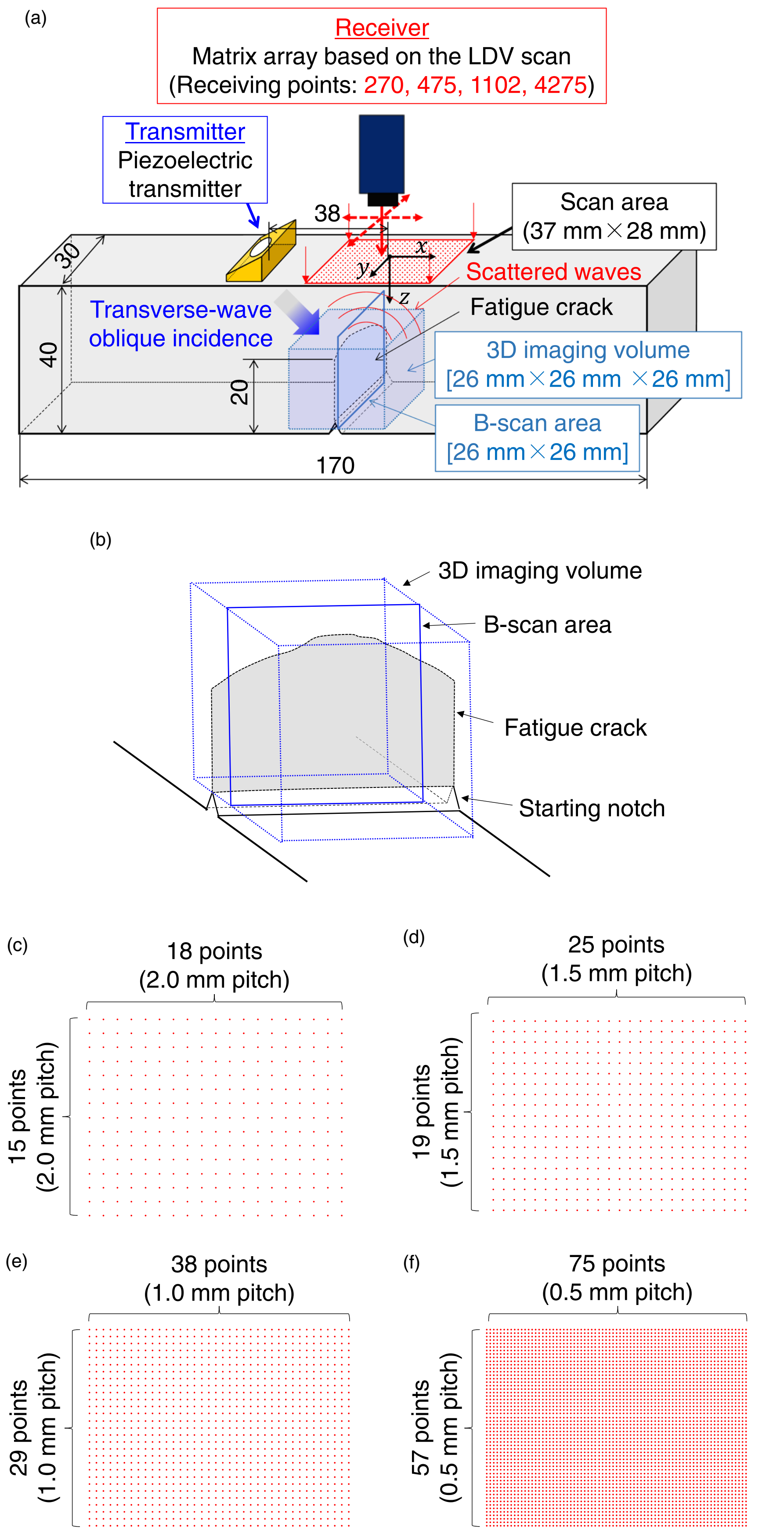

Fig. 5. (Color online) Experimental conditions for imaging the fatigue crack by the PLUS. (a) Experimental configuration. (b) Schematic illustration of the fatigue crack. Receiving points within the scan area of 37 mm × 28 mm: (c) 270, (d) 475, (e) 1102, and (f) 4275.

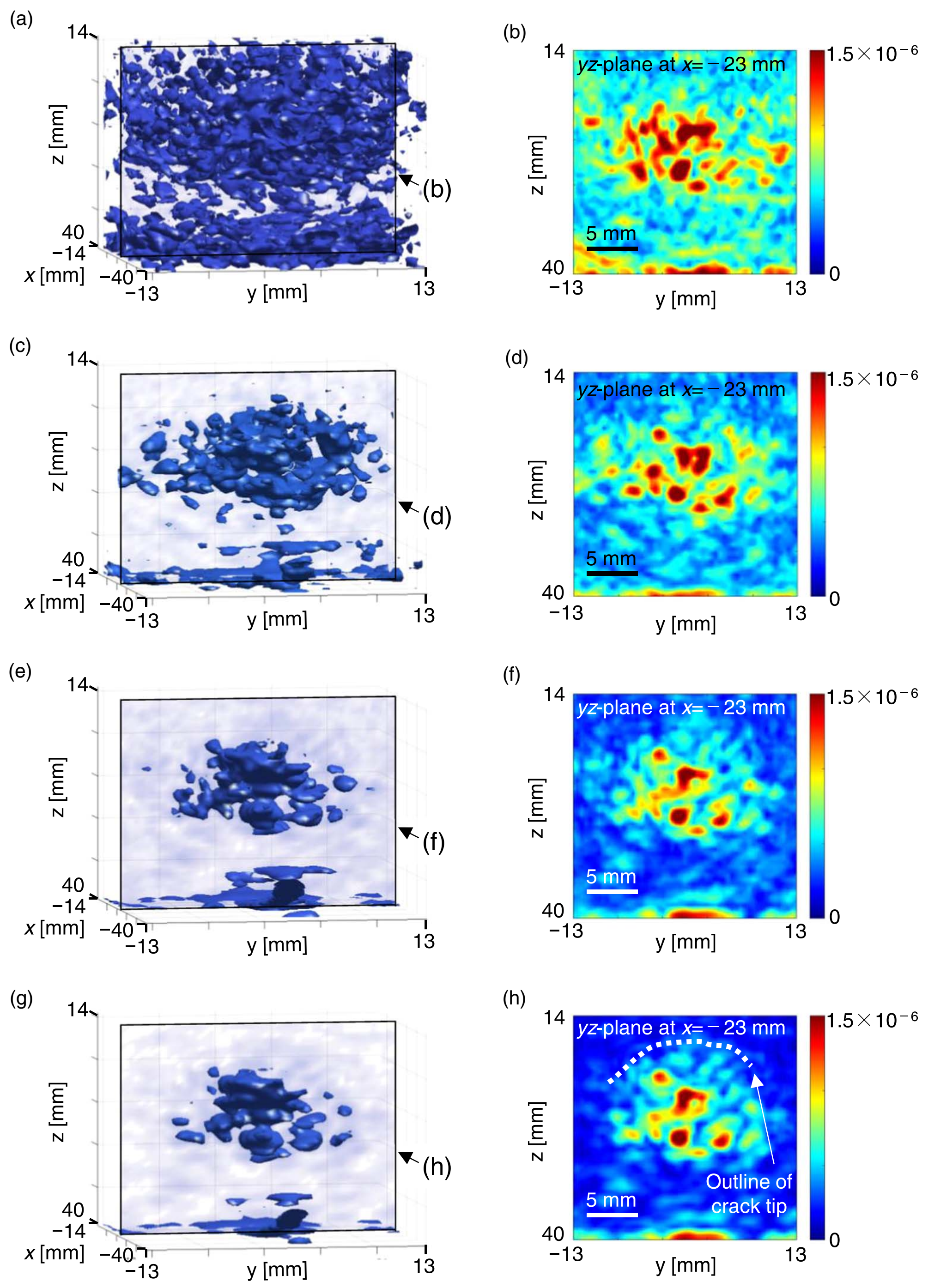

Fig. 6. (Color online) 3D imaging results of the fatigue-crack specimen obtained by the PLUS. (a) 3D view for 18 × 15 (i.e. 270 receiving points). (b) B-scan (yz-plane at $x = -23$ mm) image extracted from (a). (c) 3D view for 25 × 19 (i.e. 475 receiving points). (d) B-scan (yz-plane at $x = -23$ mm) image extracted from (c). (e) 3D view for 38 × 29 (i.e. 1102 receiving points). (f) B-scan (yz-plane at $x = -23$ mm) image extracted from (e). (g) 3D view for 75 × 57 (i.e. 4275 receiving points). (h) B-scan (yz-plane at $x = -23$ mm) image extracted from (g).

above a threshold of 0.75×10^{-6}, which is a half of the maxmium value of the color scale for Figs. 6(b), 6(d), 6(f), and 6(h), with the semitransparent B-scan (yz-plane at $x = -23$ mm) images, which were extracted from the 3D imaging results and correspond to the plane in which the fatigue crack existed. The B-scan images are also shown as opaque images in Figs. 6(b), 6(d), 6(f), and 6(h). Note that typical B-scan images obtained with a linear array transducer are for xz-plane and are perpendicular to the plane in which crack faces exist.[6–13,15,17] Such B-scan (xz-plane) images cannot resolve the crack in the y-direction because of the elevation aperture of a linear array transducer. In contrast, arbitrary planes within the 3D imaging volume can be extracted from the 3D imaging results since PLUS utilizes the 2D matrix array receiver.

For the matrix array with 270 receiving points, much noise concealed the crack response in Fig. 6(a). In the B-scan image [Fig. 6(b)], the collection of strong responses was observed around the center, whereas the identification of the crack responses was impossible because of the low SNR. For the matrix array with 475 receiving points, the SNR in the 3D image [Fig. 6(c)] was improved from that in Fig. 6(a). However, the SNR in the B-scan image [Fig. 6(d)] was still too low to identify the crack tip and measure the crack geometry. By increasing the receiving points to 1102, the SNR was further improved, as shown in Figs. 6(e) and 6(f). The responses of the fatigue crack around the center were obvious, whereas the measurement of the crack-depth distribution in the y-direction is still challenging because of the weak responses of the crack tips. For the 2D matrix array with 4275 receiving points, the noise was suppressed well, and thereby, the fatigue crack was visualized with a high SNR, as shown in Figs. 6(g) and 6(h). Notably, the outline of the fatigue crack geometry was obtained by connecting the responses at the fatigue-crack tips in the y-direction, as denoted by a white dotted curve in Fig. 6(h). The geometry showed the maximum depth around the center in the y-direction. This result was in good agreement with fracture mechanics.[18] Thus, we demonstrated that the PLUS with ultra-multiple receiving points is useful for high-resolution, high-SNR 3D imaging of fatigue cracks.

4. Discussion

In the previous section, we demonstrated the usefulness of the PLUS with ultra-multiple receiving points for the high-resolution 3D imaging of the fatigue crack. Specifically, the SNR was strongly dependent on the number of receiving points. To understand the importance of the ultra-multiple receiving points in more detail, we discuss the suppression of grating lobes and random noise as below.

To avoid grating lobes perfectly, the scan pitch should be less than approximately half the wavelength.[5] The wavelength used in this study was approximately 0.3 mm, which was smaller than the minimum scan pitch of 0.5 mm. Note that the condition for avoiding grating lobes can be mitigated by restricting an imaging volume. In this experiment, the imaging volume was 26 mm × 26 mm × 26 mm. If we only suppose the yz-plane for simplicity, the maximum angle between the line connecting from the origin to the edge at a depth of 20 mm is approximately 33°. Under this condition, the grating lobe does not appear for the scan pitch of 0.5 mm. However, when the scan pitch is more than or equal to 1.0 mm, the effect of grating lobes can appear as artifacts. This implies that Figs. 6(a)–6(f) contained the artifacts due to grating lobes.[5] Such artifacts can cause the inaccurate measurement of crack geometry. Hence, the ultra-multiple number of receiving points is vital to avoid the artifacts due to grating lobes.

We also examined the dependence of the random noise on the number of receiving points. The random noise intensity I_N was calculated as a mean value of $I(\mathbf{r})$ in the region surrounded by white dotted squares in Figs. 4(b), 4(d), 4(f), and 4(h). Figure 7 shows the dependence of I_N on the receiving points. As a result, it was found that I_N decreased with increasing the number of receiving points. This is strongly related to the delay-and-sum processing for 3D imaging. As shown in Eq. (4), this processing involves not only the extraction of scattering intensity for a voxel but also the random noise suppression due to the averaging. The number of averaging due to the delay-and-sum processing is equal to the number of receiving points (i.e. $N_x \times N_y$). This suggests that the averaging with both an oscilloscope in the acquisition and the delay-and-sum processing after the acquisition can suppress the random noise. In this study, we intentionally selected the small numbers of averaging, i.e. 5 for the FBH and 64 for the fatigue crack, for an oscilloscope to shorten the acquisition time. Even for such small numbers of averaging with an oscilloscope, the 3D imaging results [Figs. 4(g), 4(h), 6(g), and 6(h)] for more than 4000 receiving points showed high SNRs. If necessary, the SNR could be further enhanced by increasing the number of receiving points and the number of averaging with an oscilloscope. An appropriate condition would be determined by the compromise between the acquisition time and the SNR. Note that the averaging with an oscilloscope cannot eliminate the artifacts due to grating lobes. Thus, the 2D matrix array receiver with ultra-multiple receiving points is indispensable for realizing a high-resolution and high SNR in 3D imaging.

In Fig. 6(h), the fatigue crack was visualized as the multiple responses. The outline of the crack geometry was extracted by connecting the responses of the crack tip. While the upper half of the fatigue crack was successfully visualized, the lower half was invisible. To visualize the crack faces entirely, a half-skip or one-skip mode of using reflected waves will be promising, as reported in 2D PA imaging.[36–39] Combining such skip modes with the PLUS would be an exciting topic for future work.

For the imaging of the FBH and fatigue crack, we selected a single excitation voltage, respectively. By increasing the excitation voltage with a frequency of f, the PLUS may be able to capture the nonlinear signals,[40] such as higher harmonics ($2f$, $3f$, …)[41–43] and subharmonics ($f/2$, $f/3$, …),[44–46] generated at closed cracks since the LDV has a flat reception bandwidth between 0 and 20 MHz. However, much higher SNR may be required when nonlinear signals are very weak. On the other hand, it has been reported that the fundamental response at f can exhibit nonlinearity against incident wave amplitude because of the nonlinear interaction between closed cracks and ultrasound.[47] The combination of the nonlinearity of the fundamental responses against incident wave amplitude has also been proposed for 2D PA imaging.[9,11,16,17,20,48,49] This concept can be extended to 3D PA imaging using the PLUS. This would open up a new avenue to 3D PA imaging based on nonlinear ultrasonics.

While the PLUS has strong potential as a new tool to achieve high-resolution 3D imaging, the acquisition time was long for the 2D mechanical scan of the LDV. For instance, it took more than 6 h for the acquisition process of the PLUS with approximately 4000 receiving points. The acquisition process can be accelerated with a high-speed digitizer installed on a PC instead of an oscilloscope. On the other hand, we used the He–Ne LDV with a 632.8 nm red He–Ne laser source in this study. The output power is limited to 1 mW to stay in a safe laser class 2. In contrast, an infrared LDV operated at a wavelength of 1550 nm allows a higher output power of 10 mW in laser class 1 since the laser at the wavelength is absorbed in water very quickly and does not reach the retina of the human eye.[50] The use of an infrared LDV can decrease the number of averaging to shorten the acquisition time. Furthermore, large-amplitude ultrasonic incidence could increase the response of the defects. To this end, the special transmitters[51,52] that have been developed for nonlinear ultrasonic measurement would be promising and can be used as the transmitter for the PLUS. Thus, the above improvements could markedly enhance the SNR,

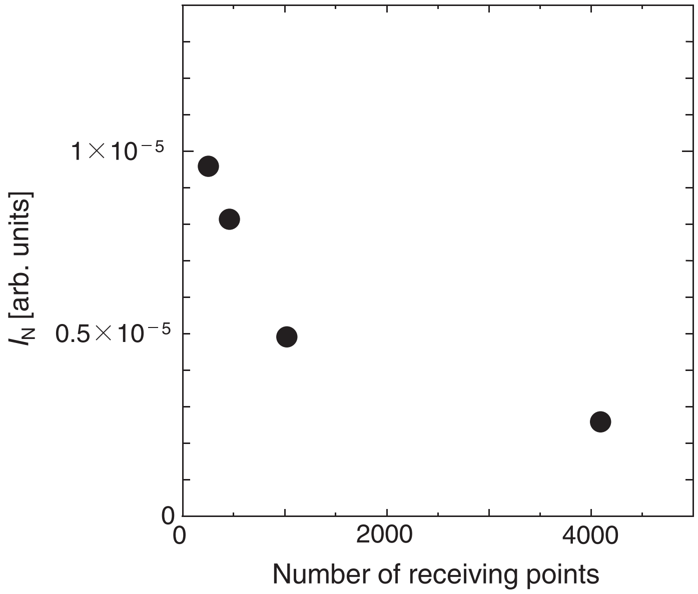

Fig. 7. Dependence of the intensities I_N of random noise on the receiving points, which were calculated as the mean intensity values in the region surrounded by white dotted squares in Figs. 4(b), 4(d), 4(f), and 4(h).

shortening the acquisition time significantly for industrial applications.

5. Conclusions

In this paper, we demonstrated the effectiveness of a novel PA imaging system, PLUS, for the high-resolution 3D imaging of fatigue cracks. The PLUS combines a piezoelectric transmitter and the 2D mechanical scan of an LDV, enabling the 2D matrix array with thousands of receiving points. After confirming the fundamental performance of the PLUS in the FBH specimen, we visualized the fatigue crack by the PLUS with varying the number of receiving points for a large receiving aperture. By increasing the number of receiving points, the SNRs in the 3D imaging results were significantly improved. Using a matrix array with 4275 receiving points, we succeeded in a high SNR, high-resolution 3D imaging of the fatigue crack, providing the 3D geometry of the fatigue crack. We also discussed the importance of ultra-multiple receiving points for suppressing grating lobes and random noise. Thus, we demonstrated that the PLUS with ultra-multiple receiving points is effective in achieving both high-resolution and high SNR in the 3D imaging of fatigue cracks.

Acknowledgments

This work was partially supported by JSPS KAKENHI (19K21910, 21H04592) and JST FOREST program (JPMJFR2023).

1) J. Blitz and G. Simpson, *Ultrasonic Methods of Non-destructive Testing* (Springer, Berlin, 1995).
2) L. W. Schmerr, *Fundamentals of Ultrasonic Nondestructive Evaluation* (Springer, Berlin, 1998).
3) B. W. Drinkwater and P. D. Wilcox, NDT E Int. **39**, 525 (2006).
4) L. W. Schmerr, *Fundamentals of Ultrasonic Phased Arrays* (Springer International Publishing, Cham, 2015) Vol. 215.
5) S. Wooh and Y. Shi, Ultrasonics **36**, 737 (1998).
6) Y. Ohara, T. Mihara, R. Sasaki, T. Ogata, S. Yamamoto, Y. Kishimoto, and K. Yamanaka, Appl. Phys. Lett. **90**, 011902 (2007).
7) S. Horinouchi, M. Ikeuchi, Y. Shintaku, Y. Ohara, and K. Yamanaka, Jpn. J. Appl. Phys. **51**, 07GB15 (2012).
8) Y. Ohara, J. Potter, H. Nakajima, T. Tsuji, and T. Mihara, Jpn. J. Appl. Phys. **58**, SGGB06 (2019).
9) Y. Ohara, T. Umezaki, E. Carcreff, S. Haupert, T. Tsuji, and T. Mihara, Jpn. J. Appl. Phys. **60**, SDDB01 (2021).
10) Y. Ohara, K. Takahashi, S. Murai, and K. Yamanaka, Appl. Phys. Lett. **103**, 031917 (2013).
11) J. N. Potter, A. J. Croxford, and P. D. Wilcox, Phys. Rev. Lett. **113**, 144301 (2014).
12) Y. Ohara, K. Takahashi, K. Jinno, and K. Yamanaka, Mater. Trans. **55**, 1003 (2014).
13) K. Takahashi, K. Jinno, Y. Ohara, and K. Yamanaka, Jpn. J. Appl. Phys. **53**, 07KC20 (2014).
14) K. Jinno, A. Sugawara, Y. Ohara, and K. Yamanaka, Mater. Trans. **55**, 1017 (2014).
15) Y. Ohara, K. Takahashi, Y. Ino, K. Yamanaka, T. Tsuji, and T. Mihara, NDT E Int. **91**, 139 (2017).
16) S. Haupert, Y. Ohara, E. Carcreff, and G. Renaud, Ultrasonics **96**, 132 (2019).
17) Y. Ohara, H. Nakajima, S. Haupert, T. Tsuji, and T. Mihara, J. Acoust. Soc. Am. **146**, 266 (2019).
18) T. L. Anderson, *Fracture Mechanics: Fundamentals and Applications* (CRC Press, Boca Raton, FL, 2005).
19) Y. Ohara, H. Endo, M. Hashimoto, Y. Shintaku, and K. Yamanaka, AIP Conf. Proc. **1211**, 903 (2010).
20) Y. Ohara, H. Nakajima, S. Haupert, T. Tsuji, and T. Mihara, Jpn. J. Appl. Phys. **59**, SKKB01 (2020).
21) K. S. Chan, Int. J. Fatigue **32**, 1428 (2010).
22) M. Ambati, T. Gerasimov, and L. De Lorenzis, Comput. Mech. **55**, 1017 (2015).
23) J. Vrana and R. Singh, J. Nondestruct. Eval. **40**, 61 (2021).
24) O. Martinez, M. Akhnak, L. G. Ullate, and F. M. De Espinosa, NDT E Int. **36**, 57 (2003).
25) A. Baba, N. Kono, S. Kitazawa, Y. Adachi, M. Odakura, and O. Kikuchi, AIP Conf. Proc. **1211**, 941 (2010).
26) C. Lane, *The Development of a 2D Ultrasonic Array Inspection for Single Crystal Turbine Blades* (Springer, Berlin, Cham, 2013).
27) J. G. Mckee, R. L. T. Bevan, P. D. Wilcox, and R. E. Malkin, NDT E Int. **113**, 102260 (2020).
28) J. Provost, C. Papadacci, J. E. Arango, M. Imbault, M. Fink, J. L. Gennisson, M. Tanter, and M. Pernot, Phys. Med. Biol. **59**, L1 (2014).
29) C. Rabut, M. Correia, V. Finel, S. Pezet, M. Pernot, T. Deffieux, and M. Tanter, Nat. Methods **16**, 994 (2019).

30) Y. Ohara, M. C. Remillieux, T. Onuma, K. Tsunoda, T. Tsuji, and T. Mihara, Appl. Phys. Lett. **117**, 111902 (2020).
31) Y. Ohara, M. C. Remillieux, T. J. Ulrich, S. Ozawa, K. Tsunoda, T. Tsuji, and T. Mihara, Proc. Symp. Ultrason. Electron **42**, 2Pb2–6 (2021).
32) D. Lévesque, A. Blouin, C. Néron, and J. P. Monchalin, Ultrasonics **40**, 1057 (2002).
33) S. Yamamoto, T. Hoshi, T. Miura, J. Semboshi, M. Ochiai, Y. Fujita, T. Ogawa, and S. Asai, Mater. Trans. **55**, 998 (2014).
34) D. Lévesque, Y. Asaumi, M. Lord, C. Bescond, H. Hatanaka, M. Tagami, and J. P. Monchalin, Ultrasonics **69**, 236 (2016).
35) J. W. Goodman, *Introduction to Fourier Optics* (Roberts and Company Publishers, Englewood, 2004) 3rd ed..
36) L. Le Jeune, S. Robert, E. Lopez Villaverde, and C. Prada, Ultrasonics **64**, 128 (2016).
37) J. Zhang, B. W. Drinkwater, P. D. Wilcox, and A. J. Hunter, NDT E Int. **43**, 123 (2010).
38) M. V. Felice, A. Velichko, and P. D. Wilcox, NDT E Int. **68**, 105 (2014).
39) N. Budyn, R. L. T. Bevan, J. Zhang, A. J. Croxford, and P. D. Wilcox, IEEE Trans. Ultrason. Ferroelectr. Freq. Control **66**, 1129 (2019).
40) K.-Y. Jhang, C. J. Lissenden, I. Solodov, Y. Ohara, and V. Gusev, *Measurement of Nonlinear Ultrasonic Characteristics* (Springer, Berlin, Singapore, 2020).
41) O. Buck, W. L. Morris, and J. M. Richardson, Appl. Phys. Lett. **33**, 371 (1978).
42) Y. Ohara and K. Kawashima, Jpn. J. Appl. Phys. **43**, 3119 (2004).
43) T. J. Ulrich, A. M. Sutin, T. Claytor, P. Papin, P. Y. Le Bas, and J. A. TenCate, Appl. Phys. Lett. **93**, 151914 (2008).
44) I. Y. Solodov, Ultrasonics **36**, 383 (1998).
45) Y. Ohara, T. Mihara, and K. Yamanaka, Ultrasonics **44**, 194 (2006).
46) K. Yamanaka, Y. Ohara, M. Oguma, and Y. Shintaku, Appl. Phys. Express **4**, 076601 (2011).
47) M. Scalerandi, A. S. Gliozzi, C. L. E. Bruno, D. Masera, and P. Bocca, Appl. Phys. Lett. **92**, 32 (2008).
48) M. Ikeuchi, K. Jinno, Y. Ohara, and K. Yamanaka, Jpn. J. Appl. Phys. **52**, 07HC08 (2013).
49) Y. Ohara, H. Nakajima, T. Tsuji, and T. Mihara, NDT E Int. **108**, 102170 (2019).
50) A. Dräbenstedt, J. Sauer, and C. Rembe, AIP Conf. Proc. **1457**, 113 (2012).
51) T. Mihara, T. Hamajima, H. Tashiro, and A. Sato, AIP Conf. Proc. **1511**, 1617 (2013).
52) T. Mihara, G. Konishi, Y. Miura, and H. Ishida, AIP Conf. Proc. **1581**, 727 (2014).